



A Population of Dipper Stars from the Transiting Exoplanet Survey Satellite Mission

Benjamin K. Capistrant^{1,2}, Melinda Soares-Furtado^{1,16}, Andrew Vanderburg^{1,3}, Marina Kounkel⁴, Saul A. Rappaport³, Mark Omohundro⁵, Brian P. Powell⁶, Robert Gagliano⁷, Thomas Jacobs⁸, Veselin B. Kostov^{6,9,10}, Martti H. Kristiansen¹¹, Daryll M. LaCourse¹², Allan R. Schmitt¹³, Hans Martin Schwengeler¹⁴, and Ivan A. Terentev¹⁵

¹ Department of Astronomy, University of Wisconsin-Madison, 475 N. Charter Street, Madison, WI, 53703, USA; bcapistrant@ufl.edu

² Department of Astronomy, University of Florida, Gainesville, FL, 32611, USA

³ Department of Physics and Kavli Institute for Astrophysics and Space Research, Massachusetts Institute of Technology, Cambridge, MA, 02139, USA

⁴ Department of Physics and Astronomy, Vanderbilt University, VU Station 1807, Nashville, TN, 37235, USA

⁵ Citizen Scientist, c/o Zooniverse, Department of Physics, University of Oxford, Denys Wilkinson Building, Keble Road, Oxford, OX1 3RH, UK

⁶ NASA Goddard Space Flight Center, 8800 Greenbelt Road, Greenbelt, MD, 20771, USA

⁷ Amateur Astronomer, Glendale, AZ, USA

⁸ Amateur Astronomer, 12812 SE 69th Place, Bellevue, WA, USA

⁹ SETI Institute, 189 Bernardo Ave, Suite 200, Mountain View, CA 94043, USA

¹⁰ GSFC Sellers Exoplanet Environments Collaboration

¹¹ Brorfelde Observatory, Observator Gyldenkeres Vej 7, DK-4340 Tølløse, Denmark

¹² Amateur Astronomer, 7507 52nd Place NE, Marysville, WA 98270, USA

¹³ Citizen Scientist, 616 W. 53rd Street, Apt. 101, Minneapolis, MN 55419, USA

¹⁴ Citizen Scientist, Planet Hunter, Bottmingen, Switzerland

¹⁵ Citizen Scientist, Planet Hunter, Petrozavodsk, Russia

Received 2021 December 13; revised 2022 September 2; accepted 2022 September 5; published 2022 November 9

Abstract

Dipper stars are a classification of young stellar objects that exhibit dimming variability in their light curves, dropping in brightness by 10%–50%, likely induced by occultations due to circumstellar disk material. This variability can be periodic, quasiperiodic, or aperiodic. Dipper stars have been discovered in young stellar associations via ground-based and space-based photometric surveys. We present the detection and characterization of the largest collection of dipper stars to date: 293 dipper stars, including 234 new dipper candidates. We have produced a catalog of these targets, which also includes young stellar variables that exhibit predominately burst-like variability and symmetric variability (equal parts bursting and dipping). The total number of catalog sources is 414. These variable sources were found in a visual survey of TESS light curves, where dip-like variability was observed. We found a typical age among our dipper sources of <5 Myr, with the age distribution peaking at ≈ 2 Myr, and a tail of the distribution extending to ages older than 20 Myr. Regardless of the age, our dipper candidates tend to exhibit infrared excess, which is indicative of the presence of disks. TESS is now observing the ecliptic plane, which is rich in young stellar associations, so we anticipate many more discoveries in the TESS data set. A larger sample of dipper stars would enhance the census statistics of light-curve morphologies and dipper ages.

Unified Astronomy Thesaurus concepts: [Variable stars \(1784\)](#); [Pre-main sequence \(1289\)](#); [T Tauri stars \(252\)](#); [Photometry \(1234\)](#)

Supporting material: machine-readable table

1. Introduction

The variability of young stellar objects (YSOs) is extremely diverse, owing to a wide range of physical processes that are germane to the early phases of stellar evolution. This includes chromospheric activity, the active accretion from circumstellar material that may generate hot spots and bursting activity, and occultations from a dusty circumstellar disk (Cody et al. 2014). Among the classes of YSO variables are *dipper stars*, a subclass of T Tauri stars that exhibit episodic or quasiperiodic dimming events where the brightness drops by $\sim 10\%$ – 50% (e.g., Alencar et al. 2010; Cody & Hillenbrand 2010; Morales-Calderón et al. 2011; Cody et al. 2014; Stauffer et al. 2015; Ansdell et al. 2016; Rodriguez et al. 2017; Cody &

Hillenbrand 2018; Hedges et al. 2018; Bredall et al. 2020; Roggero et al. 2021; Venuti et al. 2021).

The vast majority of cataloged dipper stars are K and M dwarfs and are therefore low in mass. The dimming events generally occur over short timescales, ranging from hours to days, with obvious changes in both the shape and depth of the dips. These sources have also been shown to exhibit burst-like signatures in addition to dips in brightness (e.g., Cody et al. 2014; Hedges et al. 2018; Bredall et al. 2020).

Dipper stars have been detected over the past two decades via ground-based and space-based photometric instruments and surveys (optical and infrared) including the Convection, Rotation and Planetary Transits satellite (CoRoT; Baglin et al. 2006; Auvergne et al. 2009), the Spitzer Infrared Array Camera (Fazio et al. 2004; Werner et al. 2004), KELT (Pepper et al. 2007), Kepler/K2 (Borucki et al. 2010; Howell et al. 2014), TESS (Ricker et al. 2015), the All-Sky Automated Survey for Supernovae (ASAS-SN; Kochanek et al. 2017), and The Next Generation Transit Survey (NGTS; Wheatley et al. 2018).

¹⁶ NASA Hubble Postdoctoral Fellow.

One possible mechanism driving the dipping phenomenon is the presence of dust occultations from the inner regions of a nearly edge-on circumstellar disk (e.g., Stauffer et al. 2015; Bodman et al. 2017). It has also been noted that some dippers are capable of exhibiting periodic features at the stellar rotation frequency if the disk-truncation radius is near the corotation radius (Bouvier et al. 2007; Alencar et al. 2018). The presence of a nearly edge-on circumstellar disk is supported by spectroscopic and spectropolarimetric observations (e.g., Bouvier et al. 2003; Alencar et al. 2010). We refer the reader to Roggero et al. (2021) for an up-to-date and detailed discussion of the mechanisms driving the dipper phenomenon.

Over 500 dipper candidates have been cataloged to date. Moulton (2020) provides an in-depth review of dipper star detections and their corresponding catalogs. Dipper stars are generally members of young associations and have been detected within a number of young comoving systems, including ρ Ophiuchus (1 Myr) (e.g., Ansdell et al. 2016); the Orion Nebula Cluster (1–3 Myr) (e.g., Morales-Calderón et al. 2011; Moulton 2020; Tajiri et al. 2020, Moulton et al. 2022); the Lagoon nebula (1–3 Myr); the Lupus region (1–3 Myr) (e.g., Bredall et al. 2020; Nardiello 2020); the Taurus association (3 Myr) (e.g., Rodriguez et al. 2017; Rebull et al. 2020; Roggero et al. 2021); the open cluster NGC 2264 (3 Myr) (e.g., Alencar et al. 2010; Cody et al. 2014); γ Velorum (3–4 Myr) (Nardiello 2020); Chamaeleon I and II (both 3 Myr) (e.g., Frasca et al. 2020; Nardiello 2020); Upper Scorpius (5–10 Myr) (e.g., Ansdell et al. 2016; Cody & Hillenbrand 2018; Tajiri et al. 2020); and the Corona Australis association (<10 Myr) (Nardiello 2020).

The population of dipper stars in NGC 2264 comprises 20%–30% of all classical T Tauri cluster members (Alencar et al. 2010; Cody et al. 2014), as well as 30% of disk-bearing stars in the Taurus cluster (Roggero et al. 2021). The mechanism driving this dipping phenomenon in NGC 2264 was investigated by Stauffer et al. (2015), where they determined the dimming to be induced by disk occultations at/near the corotation radius.

The detection of more candidates is necessary to understand better the relationship between light-curve morphologies, stellar characteristics (mass, age, etc.), and circumstellar disk characteristics. In addition, dipper stars have much to offer low-mass, pre-main-sequence stellar models, including the role of flares (e.g., Favata et al. 2005), the shape and mass distribution within the inner circumstellar disk (e.g., Bouvier et al. 1999), and the evolution of the circumstellar and protoplanetary disks (e.g., Bodman et al. 2017). We refer the reader to Bodman et al. (2017) for a detailed discussion of the stellar constraints and diagnostics provided by dipper stars.

To expand the population of dipper catalog sources, we searched through millions of TESS light curves to identify and characterize dipper star candidates. In this work, we report the discovery of 234 new dipper stars and examine their age and membership demographics. In Section 2, we describe our variable star data set and illustrate the light curves of several targets. In Section 3, we present our vetting and classification methods, including our methods to quantify light-curve morphology and provide stellar age estimations. In Section 4, we present the results of our calculations. In Section 5, we summarize our findings and discuss prospects to expand the dipper candidate population further.

2. Data

2.1. Premade Light Curves of Targets

We searched for compelling dipper stars by visual inspection of millions of TESS light curves. The light curves used in this study come from a number of different sources, which are described below. These include the Cluster Difference Imaging Photometric Survey (CDIPS; Bouma et al. 2019), MIT Quick Look Pipeline (QLP; Huang et al. 2020a, 2020b), PSF-based Approach to TESS High quality data Of Stellar clusters (PATHOS; Nardiello et al. 2019), the NASA Goddard Space Flight Center Eclipsing Binary survey (GSFC EB; Powell et al. 2022), difference-imaging extracted light curves from Oelkers & Stassun (2019), and the Science Processing Operations Center (SPOC; Jenkins et al. 2016). Each of these databases makes use of TESS full frame images (FFIs), except for SPOC which uses 2 minutes and 20 s target pixel files (TPFs).

1. CDIPS: the CDIPS team creates light curves from TESS FFIs with 30 minute cadences using difference imaging (also commonly referred to as image subtraction). They target stars in open clusters, moving groups, as well as stars that show evidence of youth. The cdips-pipeline provides light curves for stars brighter than a Gaia magnitude of 16 with 20–25 day observation windows (Bhatti et al. 2019).
2. QLP: the MIT QLP team uses the MIT quick look pipeline to create light curves from TESS FFIs for stars brighter than a TESS magnitude (T_{mag}) of 13.5. In support of the team’s primary goal of generating light curves for promising exoplanet candidates, they provide single-sector light curves for targets observed over the TESS Primary Mission, including Sectors 1–26, and now the first year of the TESS Extended Mission, Sectors 27 through 39. Targets from the second year of the TESS Extended Mission are to be released in 2022.
3. PATHOS: the PATHOS project uses empirical point spread functions (PSFs) to obtain light curves from TESS FFIs by minimizing dilution effects in crowded environments. Their methodology also includes aperture photometry to compare with their PSF fitting methods. Their typical targets are stars in the faint regime ($T_{\text{mag}} > 13$ mag), and they focus on clusters that include many young stars.
4. GSFC EB Survey: some of our team members from the NASA Goddard Space Flight Center (GSFC) Astrophysics Science Division are responsible for the production of TESS FFI light curves for stars $T_{\text{mag}} < 15$ mag (in this paper, we refer to this sample as “GSFC”). A parallelized implementation of the `eleanor` Python module is then performed on all sources (Feinstein et al. 2019), and a catalog of eclipsing binaries is generated using a neural network classifier. In addition to the identification of eclipsing binaries, some dipper candidates were culled from this effort. We refer the interested reader to Section 2 of Powell et al. (2021) to learn more about the GSFC light-curve reduction and classification effort.
5. Oelkers & Stassun Sample: Oelkers & Stassun (2019) publicly released a population of TESS FFI light curves, which were reduced using a difference imaging technique that is described in Oelkers & Stassun (2018). The target sources were extracted from the TESS Input Catalog. The reduced light curves achieve a noise floor of 60 ppm $\text{hr}^{-1/2}$.

These light curves are available on the Filtergraph data visualization platform.¹⁷

6. SPOC: The Science Processing Operations Center (SPOC) at NASA Ames Research Center processes data to generate a variety of information on-target stars, including the light curves investigated in this study. The reduction pipeline processes raw pixels, extracting photometry and astrometry for each target and correcting for systematic errors. The pipeline catalogs target stars and includes their corresponding characteristics and pixel data (Jenkins et al. 2016). In contrast to the other pipelines, the SPOC pipeline uses stationary aperture photometry to generate light curves, focusing on individual target files with 2 minutes or 20 s data rather than FFIs.

2.2. Identification of Variable Star Candidates

As part of the Visual Survey Group (VSG) collaboration, several of us performed a visual inspection of millions of these light curves. The VSG is responsible for a number of discoveries using Kepler, K2, and TESS data sets (e.g., Schmitt et al. 2016; Mann et al. 2020; Powell et al. 2021; Kristiansen et al. 2022). To identify dipper candidates (among other variable star classes), the VSG team uses a Windows-based publicly available software system known as `LcTools` (Schmitt et al. 2019; Schmitt & Vanderburg 2021). `LcTools` provides users with three principal tools: `LcGenerator` to create normalized light curves in bulk, `LcSignalFinder` to find and record candidate signals (periodic and aperiodic) automatically in large sets of light curves, and `LcViewer` to inspect light curves visually for candidate signals. We identified a total of 477 dipper star candidates from our survey of these data sets.

3. Methods

3.1. Identifying Sources of Dipping Variability

Our dipper candidates come from several high-level science products with differing reduction techniques, making it critical to confirm light-curve variability for all sources. Because TESS has large pixels ($\sim 20''$) blending from nearby sources is common, making it difficult to identify primary sources of variability.

We therefore performed our analysis to identify blended signals using the publicly available `Lightkurve` python package (Lightkurve Collaboration et al. 2018). We constructed and inspected customized light curves for the dipper star candidates using TPF¹⁸ cutouts from the TESS FFIs, generated by the `TESSCut` software¹⁹ (Brasseur et al. 2019). `TESSCut` returns pixel time series from regions of the TESS FFIs in the vicinity of a target star. These cutout images allow for detailed inspection of the star’s light in a given observation and the production of custom light curves. To generate these light curves, we employed customized apertures, which mitigate blending from neighboring stars and can be used to identify the target responsible for the variability signal more carefully.

To generate light curves for our candidates, we first selected the pixel where the target star is located, masking surrounding

pixels to isolate the flux coming from the target. For pixel selection, we use the World Coordinate System (WCS) included in the metadata of the `TessTargetPixelFile` objects. The WCS parameters in the fits headers provide information on how the pixels map to celestial coordinates, which we use to locate the target star within a given TPF.

We chose to customize our apertures for our targets because the `Lightkurve` package’s built-in methods do not consistently mask the appropriate target star, especially when the target star is fainter than close-by companions. This is because the method relies on a set flux threshold, which does not always contain the target star. We chose the smallest possible aperture to confirm that the dipping variability is on or off-target. We identified the pixel closest to the location of the star, and then employed the `Lightkurve` function `tpf.to_lightcurve()` to create a light curve from the isolated pixel, subtracting the light curve generated from the background pixels. Figure 1 shows six light curves from our sample generated with our TPF masking method.

We classified stars as on-target if the variability in our masked TPF light curves closely matched the variability in the pregenerated light curves. Similarly, sources were classified as off-target when the variability did not match. The on/off-target determination was performed by eye, with each source visually inspected by three different individuals. We classified 414 of the dipper candidates as on-target, and use these as our catalog going forward. An example of both the on- and off-target stars can be found in Figure 2.

3.2. Light-curve Flux Asymmetry Classification

Once we obtained the on-target star candidates, we classified their variability. We categorized the variable stars as bursting, symmetric, or dipping, which are descriptors defined by the flux asymmetry with respect to reflection along the flux axis of its light curve. To determine the light-curve flux asymmetry of our target stars, we calculated the M metric, which is described in more detail in Cody et al. (2014). Following their methodology, we first subtracted a smoothed version of the light curve generated by a boxcar with a width of 10 days. We then clipped 5σ outliers from the boxcar-smoothed light curve. After taking the mean of the top 10% and bottom 10% flux values from the residual light curve, we find the asymmetry metric, M , given by

$$M = \frac{\langle d_{10\%} \rangle - d_{\text{med}}}{\sigma_d}, \quad (1)$$

where $\langle d_{10\%} \rangle$ is the top and bottom decile mean, d_{med} is the median of the long-term trend and outlier-removed light-curve flux, and σ_d is the standard deviation. Cody et al. (2014) found that the M metric is only sensitive to timescales below 15–20 days.

We remove long-term stellar variability and instrumental artifacts by smoothing our light curves with the `keplersplinev2`²⁰ tool (Vanderburg & Johnson 2014). We employed a spline knot spacing of 10 days, and subtracted the best-fitting spline from the original light curve before computing the M metric. While `keplersplinev2` was produced to work with the Kepler data set, this tool also works well with the TESS data set. Figure 1 displays the light curves of six on-target

¹⁷ https://filtergraph.com/tess_ffi

¹⁸ <https://heasarc.gsfc.nasa.gov/docs/tess/Target-Pixel-File-Tutorial.html>

¹⁹ <https://mast.stsci.edu/tesscut/>

²⁰ <https://github.com/avanderburg/keplersplinev2>

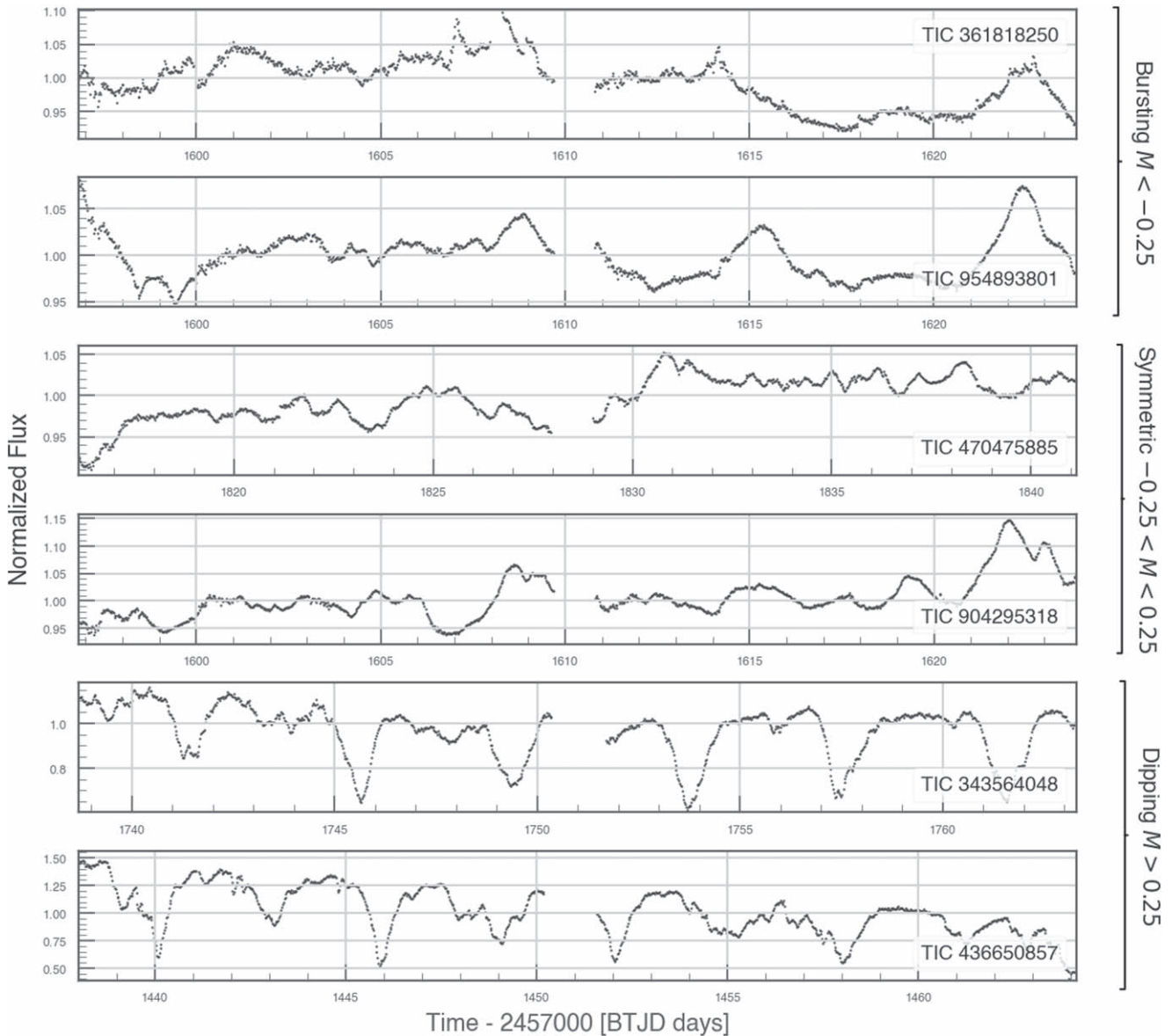


Figure 1. Our custom light curves corresponding to six on-target dipper candidates. Included are TICs 361818250, 954893801, 470475885, 904295318, 343564048, and 436650857. Light curves were generated after isolating candidates in their TPFs. We opted to illustrate a range of flux asymmetry M classifications as described in Section 3.2. The top two light curves are examples of the predominately “bursting” flux asymmetry ($M < -0.25$), rows three and four illustrate sources with “symmetric” flux asymmetry ($-0.25 < M < 0.25$) and the bottom two rows illustrate sources with predominately dipping flux asymmetry ($M > 0.25$). Only sources with $M > 0.25$ are classified as dippers in our resulting catalog.

sources ranging in M metric classifications. The top two rows display sources that are predominately bursting ($M < -0.25$), the central two rows display sources that predominately symmetric ($-0.25 > M > 0.25$), and the bottom two rows display sources that are predominately dipping ($M > 0.25$). Only sources with $M > 0.25$ are classified as dippers in our resulting catalog.

3.3. Periodicity of Dipper Candidates

In this section, we describe the method for classifying the periodicity of our catalog sources by implementing a second variability metric presented by Cody et al. (2014): the periodicity metric, Q . Following their methods for comparative consistency, we computed an autocorrelation function (ACF)

on the magnitudes of each light curve to home in on the period of the source.

Before computing, we interpolated the data to fill any gaps in the time-series data. We then calculated and recorded the largest local ACF peak. To find the strongest ACF peak, we used a function from the `Scipy` Python package (Virtanen et al. 2020), specifying the following three criteria: (1) adjacent ACF peaks must be separated by a minimum of 15 points, (2) the peak prominence (a measure of the vertical distance between the peak and the surrounding baseline of the signal) must exceed 0.05, and (c) bypass the first identified ACF peak, as this feature is associated with short lags. Our peak prominence setting of 0.05 permits the identification of ACF peaks for all dipper candidates. For a highly aperiodic target, such as with white-noise time-series data, the resulting Q value

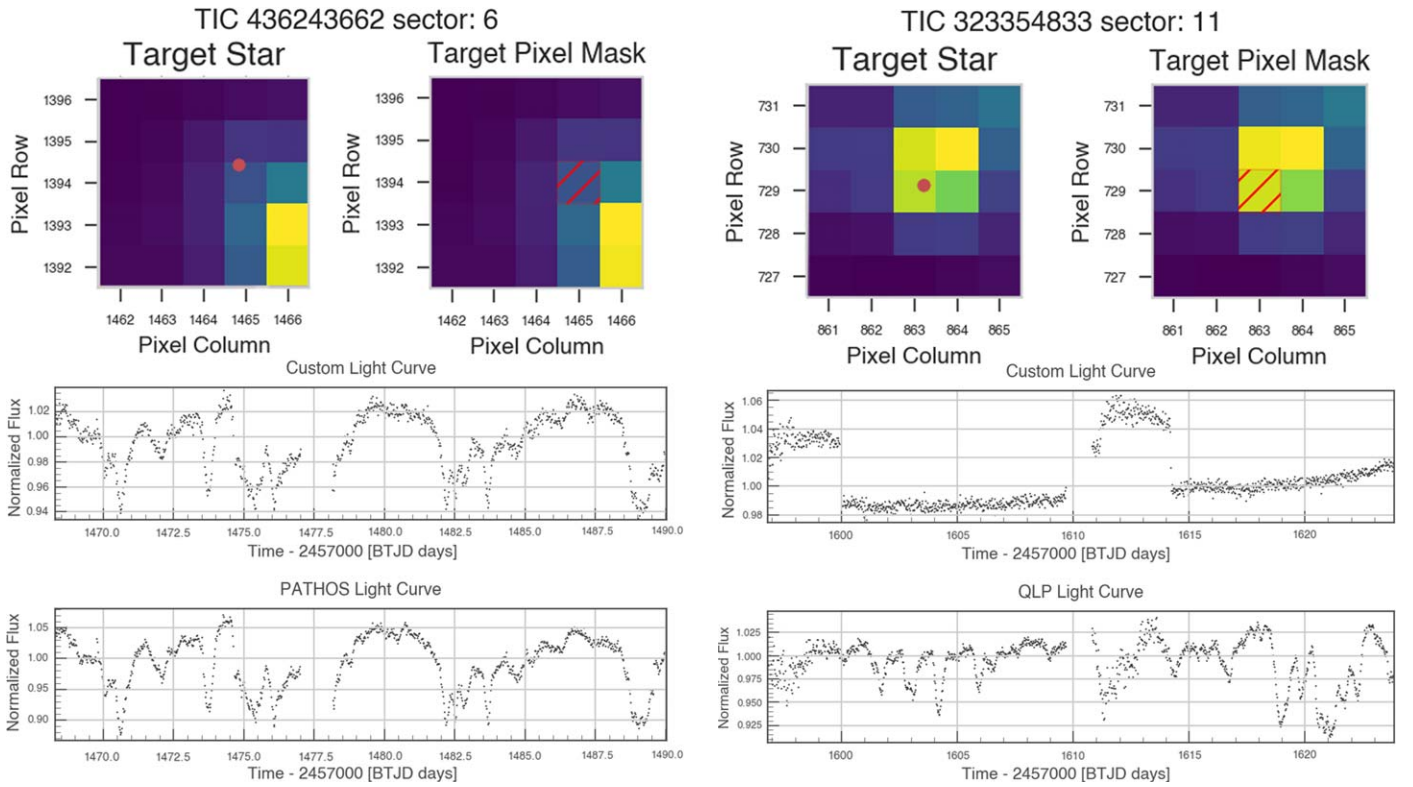


Figure 2. Example of on-target (left) and off-target (right) sources. Top row: custom apertures applied to the TESS TPFs. Middle row: light curves generated from the masked pixel with the background light curve subtracted. Bottom row: pregenerated light curves (the origins of the light curve vary depending on availability for each star). The left-hand example (TIC 436243662) shows similar variability in the pregenerated light curve and our custom light curve, consistent with the source of the variability being the target star. On the other hand, our custom single-pixel light curve in the right-hand example (TIC 323354833) does not show the same variability as the pregenerated light curve, indicating that the source of the variability may be off-target.

is near unity, which indicates aperiodic light-curve morphology. Challenges corresponding to the Q metric, particularly as it pertains to aperiodic sources, are discussed further in Section 4. This topic is also the subject of investigation in Hillenbrand et al. (2022).

To determine the best period of a given source better, we followed the ACF calculation with a periodogram search within 15% of the value identified by the peak ACF. Since our target light curves do not exhibit well-defined time variation, we measured the period of a given source using the Stellingwerf phase dispersion minimization (PDM) module (`astrobase.periodbase.spdm`) from the `Astrobase` Python package (Stellingwerf 1978). The PDM method utilizes a brute-force approach to data folding. A large ensemble of periods is considered in the folding of the data. The data are then binned and the binned variance and overall variance of each trial are computed. The ratio of the binned variance to the overall variance is calculated for each investigated period. False periods have a ratio close to unity, while this ratio is small for true periods. The PDM algorithm calculates the periodicity of time-series data without constraining the search to a pre-conceived functional form. While the PDM technique is capable of revealing box-like and sinusoidal variations, it is not limited to the detection of variations of this form. Therefore, the PDM technique is robust at detecting periodic signatures like those observed by periodic dippers, semiperiodic dippers, bursters, and heartbeat stars.

We searched for the best period for a given target using period search bounds within 15% of the value identified by the peak ACF. The strongest identified period in the resulting PDM

power spectrum was then used to generate a phase-folded light curve. We then smoothed the phase-folded light curve using a boxcar with a width that is 25% that of the period, and subtracted this boxcar from the light curve after long-term trends and 5σ outliers were removed. For an illustrated example of the process described, we refer the interested reader to Figure 28 in Cody et al. (2014).

The periodicity metric, Q , is given by

$$Q = \frac{(\text{RMS}_{\text{resid}}^2 - \sigma^2)}{(\text{RMS}_{\text{raw}}^2 - \sigma^2)}, \quad (2)$$

where $\text{RMS}_{\text{resid}}^2$ is the rms value of the light curve after the phase-folded, boxcar-smoothed light curve has been subtracted and $\text{RMS}_{\text{raw}}^2$ is the rms of the raw light curve before this subtraction. The parameter σ denotes the uncertainties which we obtain using a different method than Cody et al. (2014). To calculate this uncertainty, we employed a few different methods to determine typical relationships between the TESS magnitudes and photometric precision for each light-curve source. For the CDIPS and QLP light curves, we referred to the figures plotting the photometric precision against the TESS magnitudes. For the CDIPS light curves, we employed Figure 14 in Bouma et al. (2019), and for QLP, Figure 1 in Huang et al. (2020a). For PATHOS, we downloaded the full set of light curves from TESS Sector 1, measured the scatter in each light curve by calculating the point-to-point scatter (Aigrain et al. 2015), and produced our own plot of precision as a function of TESS magnitude.

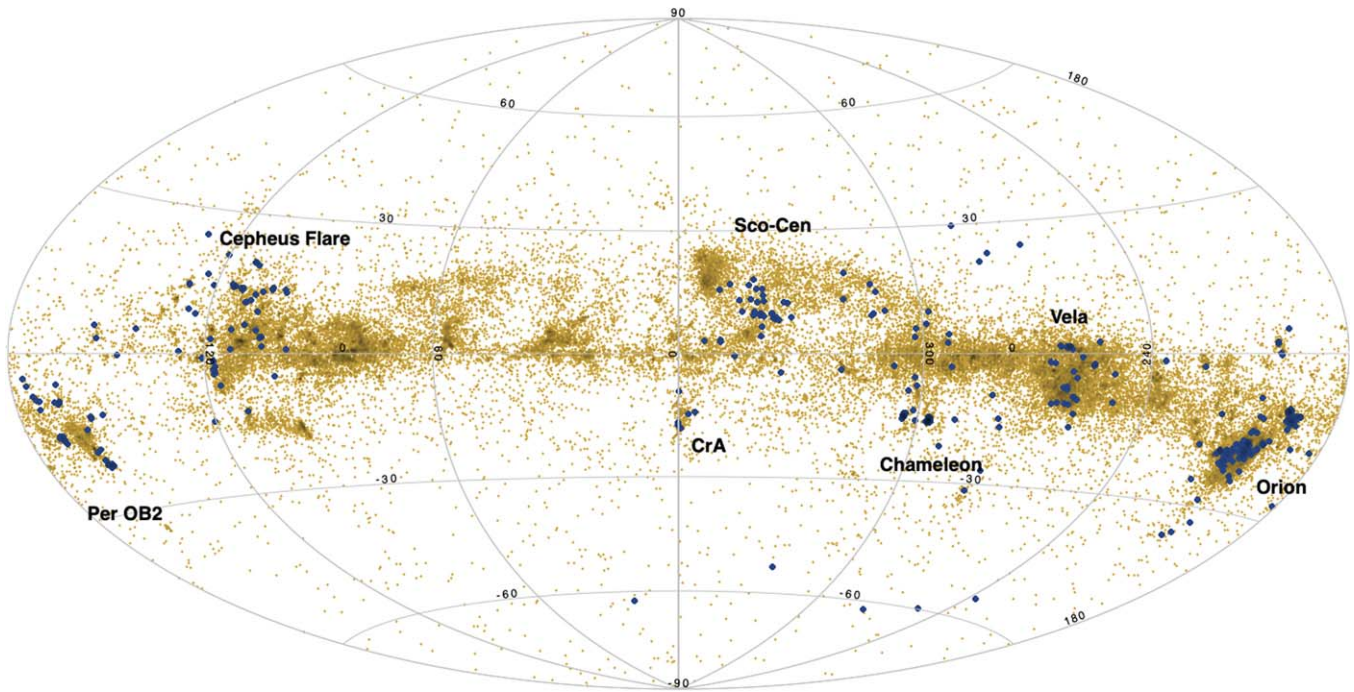


Figure 3. Spatial distribution of our catalog sources (blue) with several young stellar associations labeled. Sources in young, comoving groups are shown in gold. The distribution of our sample tracks the locations of these young stars.

We digitized each of these plots using an online plot digitizer application,²¹ obtaining the relationship between T_{mag} and precision. Authors of the CDIPS, QLP, and PATHOS pipelines gave their photometric precision measurements over timescales of 1 hr or 6 hr and assumed that the precision scaled with $1/\sqrt{\text{exposure time}}$. We converted these precision measurements to 30 minute rms values, and found the uncertainties, σ , of our candidate light curves based on their star’s T_{mag} . For the SPOC light curves, we took the full set of light curves from Sector 1, binned the two-minute-cadence light curves to 30 minute cadences, and calculated the median value of a running standard deviation filter over the full light curve. We then calculated the median photometric precision in bins as a function of TESS magnitude. Once we had relationships between T_{mag} and precision for each light-curve source, we interpolated them to the TESS band magnitude of each stellar variable to estimate the photometric precision of each light curve.

3.4. Stellar Age for Variable Stars

We compared the distribution of our catalog sources to known stellar populations. In Figure 3, we illustrate the spatial distribution of our catalog sources. We found that approximately half of our variable stars were known members of young comoving groups, as identified by Kounkel et al. (2020). Most of the other catalog sources were found in known star-forming regions and may not have been included in the comoving group catalog. Thus, to confirm their membership manually, we examined overdensities in the spatial distribution of the stellar variables in our sample toward star-forming regions such as Orion, Taurus, Sco Cen, Chameleon, and Vela.

We successfully implemented this method for a total of 371 out of 414 stars (90% of the sample). The remaining 10% of

sources were either (a) found in the vicinity of very-low-mass star-forming regions, for which it is difficult to assign membership conclusively, (b) exhibit peculiar astrometry not fully consistent with the phase space of a given population, or (c) were found to be evolved stars that contaminated the sample.

Although average ages are available for each population of comoving groups, those ages may not be accurate, due to the fact that an individual star-forming region can sustain star formation for >10 Myr (e.g., Kounkel et al. 2018; Damiani et al. 2019). As such, we opted to estimate the ages of the individual pre-main-sequence stars using the neural network *Sagitta* (McBride et al. 2021), which utilizes parallaxes, as well as Gaia and 2MASS photometry in the G, GBP, GRP, J, H, and K bands. *Sagitta* has been trained on the photometry of young stars in populations with known ages, interpolating across a sample of $\sim 70,000$ stars. This establishes an internal empirical age sequence, allowing for the minimization of systematic trends, such as those pertaining to stars of different masses having systematically different derived ages in the same cluster. It also allows us to interpret the ages for sources with significant reddening or infrared (IR) excess due to the presence protoplanetary disks, which can be difficult to place on theoretical isochrones. The trained model can then be applied to the previously unseen data to estimate ages up to $\lesssim 40\text{--}70$ Myr.

4. Results

From our initial sample of 477 light curves exhibiting variability, we determine 414 candidates to be on-target sources, which are presented in our Variable Star Catalog. As described in Section 3.1, these stars were classified as on-target when the variability in our masked TPF light curves closely matched the pregenerated light curves. We included only on-

²¹ <https://apps.automeris.io/wpd/>

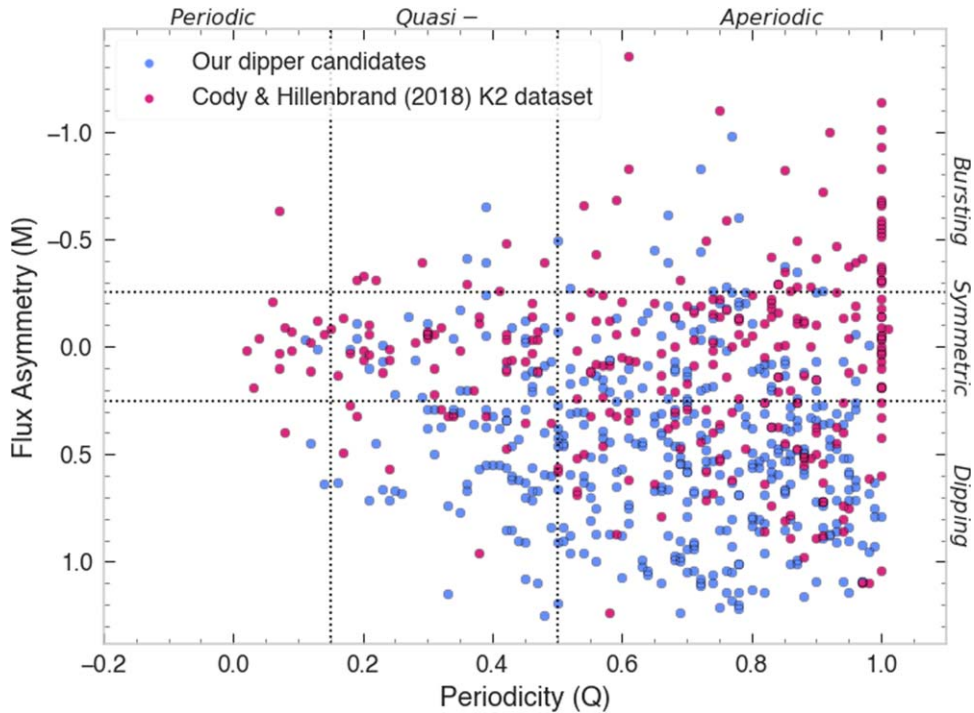


Figure 4. We plot the flux asymmetry (M) vs. periodicity (Q) metrics for our stellar variables (blue), comparing these sources to the young stellar variables analysed by Cody & Hillenbrand (2018) (red). Note that M is reflective of magnitude, and the sign of the variable is inverted from the intuitive value based on flux. Therefore, dipper stars have positive rather than negative M values. The majority of our catalog sources (70%) exhibit predominately dipping flux asymmetries. This is expected based on the search criteria of our visual survey of TESS light curves. In accordance with Cody & Hillenbrand (2018), we find no clear correlation between Q and M .

target candidates in our analyses of the morphology and ages of this population. In Table 1, we provide the first 10 rows from our Variable Star Catalog. The listed properties were obtained using data from Gaia survey data (Data Releases 2 and EDR3), as well as the TESS input catalogs (e.g., Gaia Collaboration et al. 2018; Stassun et al. 2018; Gaia Collaboration et al. 2021). Also included are our calculated M and Q variability metrics, the corresponding classification, the identification of new detections, and the estimated age of the target.

4.1. Morphology

Our catalog sources were initially flagged by the VSG as dipper candidates due to the visible dips in brightness observed in their light-curve morphologies. It is therefore not surprising that in our computation of the M and Q values, we classified the vast majority (70%) of these sources as dipper stars. Figure 1 depicts example light-curve morphologies for sources with differing values of M , including sources in the two top rows that are classified as bursters. It is important to note that the sign of the flux asymmetry, M , value is inverted from the intuitive value based on flux, as the units are reflective of magnitude. Therefore, burst-like variability corresponds to a negative M value, while dip-like variability corresponds to a positive M value.

In Figure 4, we illustrate the flux asymmetry versus periodicity of our variables. Bursters are shown in the top row, symmetric variables in the central row, and dipper stars in the bottom row. Stars classified with periodic variability are in the left column, quasiperiodic are in the central column, and those with aperiodic variability are in the right column. This figure is akin to Figure 31 in Cody et al. (2014). However, in this figure, we compare our sample to the

population investigated by Cody & Hillenbrand (2018) (red points) and refer the reader to their Figure 6, which illustrates the periodicity versus flux asymmetry of their sample. The targets from Cody & Hillenbrand (2018) are members of the Upper Sco and ρ Oph star-forming regions. In their analysis, they made no selection for light-curve morphology, and therefore their sample includes stars from all of the variability classes. The distribution of our catalog sources largely falls in the dipping region, which is in support of our expectation. In agreement with Cody et al. (2014), we find no clear correlation between the Q and M statistics.

It bears mentioning that there are challenges associated with the variability metrics, especially with generating the Q values. First, identifying peaks in the ACF, an important step in determining the Q metric, is not a straightforward process. In some cases, such as in the case of a highly aperiodic light curve, this can impact the calculations. Another difficulty arises as a result of contaminants in the light curves. Contaminants may include rapidly rotating spotted stars; pulsating stars with varying amplitudes, phases, or periods; and hot exoplanets where the transit duration is shorter than the smoothing timescale. Contaminants can result in the calculation of large Q values. Despite these complications, the Q metric is well-entrenched in scientific literature investigating YSO variability (e.g., Cody et al. 2014; Rebull et al. 2015; Cody & Hillenbrand 2018; Hillenbrand et al. 2022). We provide this metric for all our catalog variables to allow for comparison with previous and future work. Recently, Hillenbrand et al. (2022) determined that reduced cadence has a more pronounced effect on Q than photometric uncertainty, and that Q values become increasingly more inaccurate at larger, positive values.

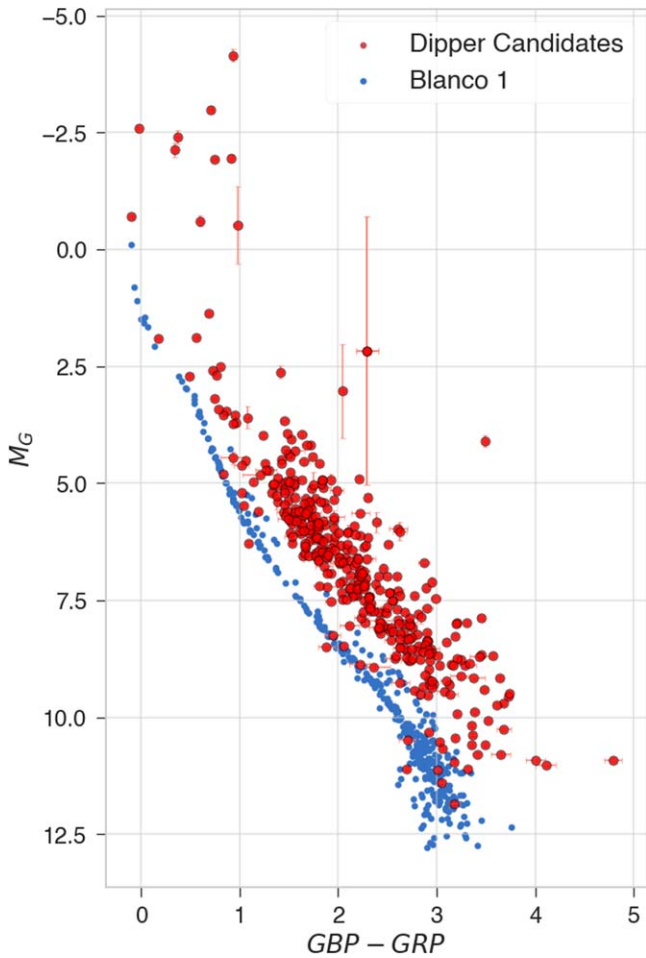


Figure 5. Diagram illustrating the dipper candidates’ GBP – GRP color against their absolute Gaia magnitude from the Gaia EDR3 catalog (415 sources shown as red points); Blanco 1 cluster (blue points) with an estimated age of 100–150 Myr (Cargile et al. 2010) are superimposed for comparison. With this figure, we can see our dipper candidates are overwhelmingly pre-main-sequence sources.

4.2. Age Distribution

We illustrate the location of our dipper candidates in the HR diagram illustrated in Figure 5. To generate this figure, we employed data from the Gaia EDR3 catalog. This figure includes a subset of our full catalog population, due to limits in the availability of Gaia EDR3 data for all sources. Most of our dipper candidates lie above the main sequence of the Blanco 1 population (blue points). Therefore, our sources are predominantly pre-main-sequence stars that are in the process of contracting onto the zero-age main sequence.

In the top panel of Figure 6, we illustrate the ages of our dipper candidates, as determined by the *Sagitta* neural network (McBride et al. 2021) (described in Section 3.4). The dipper candidates in our sample exhibit a peak in their age distribution at 2.3 Myr (red dashed line). To determine the peak age of this distribution, we fit the histogram in the top panel with a log-normal distribution. This method was also used to determine the peak age of the central panel.

Kerr et al. (2021; hereafter *K21*) derived approximate ages for $\sim 25,000$ Gaia DR2 catalog sources using photometric methods and a pipeline fully described in their study. Among the young stars in the *K21* sample, 68 targets are dipper

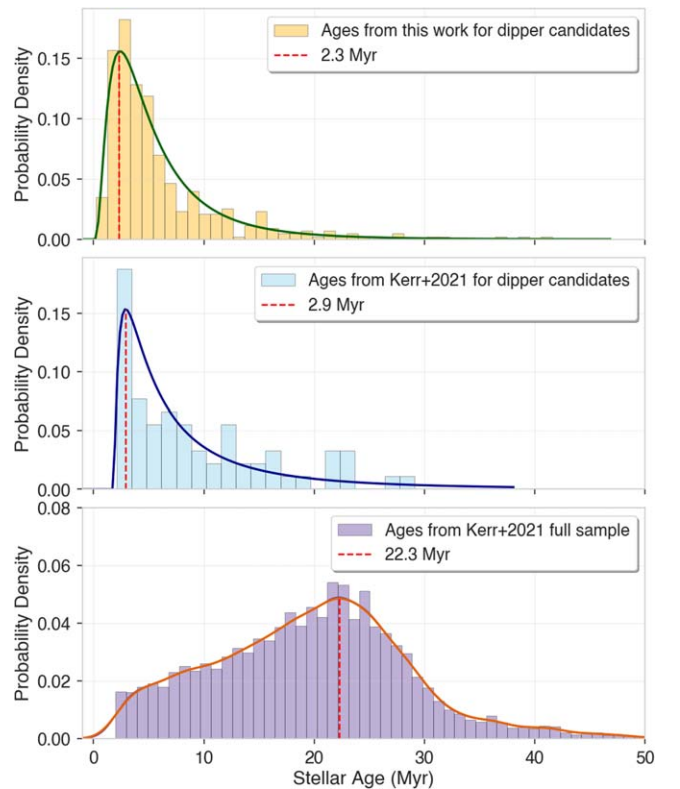


Figure 6. Top panel: ages for all of our dipper candidates (414 stars), as determined by the *Sagitta* neural network (McBride et al. 2021). Middle panel: ages for a subsample of our dipper candidates (68 stars), as derived by Kerr et al. (2021). Bottom panel: ages for the entire sample (25,324 stars) from Kerr et al. (2021) for comparison. In the top two panels, we fit the histograms with log-normal distributions to find the peak values, which we marked with a dashed red line. In the bottom panel, we used a kernel density estimate to determine the peak.

candidates found in our catalog. In the central panel of Figure 6, we illustrate a histogram of the ages, as determined by the *K21* analysis, of the overlapping *K21* subsample of 68 targets. We observed that our dipper candidates are preferentially found among the youngest stars in their sample, with the age distribution peaking at 2.9 Myr (red dashed line). In the bottom panel of Figure 6, we illustrate the age distribution of the full *K21* sample, which exhibits a much broader range of ages, peaking at 22.3 Myr. The peak in this distribution was determined using a kernel density estimate, as the full *K21* population does not exhibit a log-normal distribution.

We compare the ages of the overlapping 68 stars in the *K21* sample and our catalog in Figure 7. Overall, the distributions of ages between the two estimation methods are largely consistent within the errors. Yet, it bears mentioning that there are some systematic differences as well, largely induced by differences in the treatment of extinction in the different regions, as well as due to the different photometric bandpasses used (e.g., Gaia-only in *K21* versus Gaia+2MASS in *Sagitta*). The outlying sources where the differences between the two approaches are most pronounced tend to be concentrated in a handful of specific regions, such as the Chameleon clouds.

4.3. IR Excess

We also investigated our dipper candidates to determine if there were differences in the measurements of the IR excess, as

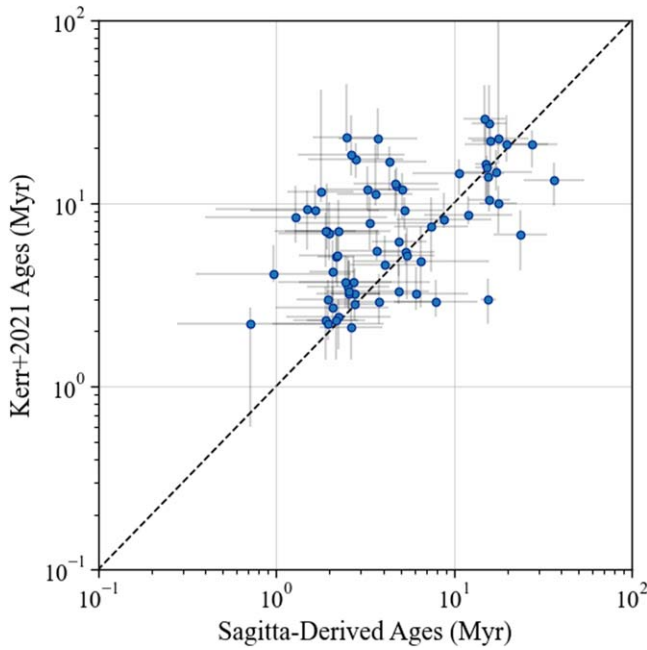


Figure 7. Scatter plot depicting the differences in the age calculations from the Sagitta neural network (McBride et al. 2021) and the K21 sample for the overlapping subset of 68 stars found in both catalogs. The dashed diagonal shows what a one-to-one age relation would be. We find for a majority of the sources that the ages derived by K21 are typically larger than those derived by Sagitta. The distribution of ages for these stars calculated by K21 can be seen in the middle panel of Figure 6.

compared to young stars (<50 Myr) that have not been flagged as candidate (or confirmed) dippers. To determine the IR excess, we combined the data from Pecaut & Mamajek (2013) and Kraus et al. (2014), establishing an expected baseline $W1 - W3$ color for young stellar sources (<50 Myr). It was necessary to combine the two data sets to ensure full coverage of the GBP - GRP range of our dipper candidates. The GBP - GRP color information was obtained from the Gaia EDR3 catalog, while the IR measurements were taken from the WISE database (Cutri et al. 2021). We then fit a second-order polynomial to the data, generating a function for the expected $W1 - W3$ color as a function of GBP - GRP. The IR excess was calculated as the difference between a given dipper candidate’s measured $W1 - W3$ color and the expected baseline $W1 - W3$ value at the corresponding GBP - GRP color.

Our results are shown in Figure 8, where we plot the IR excess of our dipper candidates as a function of their corresponding GBP - GRP color (red points). As a comparison, we created a control sample (blue points) of young stars from K21. To generate this control sample, we performed a source-by-source age match for each dipper candidate. More specifically, the control sample consists of stars that (1) have not been flagged as dipper variables in the past and (2) share a common age with a given dipper candidate (the closest age match possible within the error bounds of the K21 sample). Using these constraints, we were able to identify a corresponding K21 control star for 93% of our dipper candidates ($N = 392$).

We see that across all the GBP - GRP values, on average, our dipper candidates exhibit greater IR excess than the K21 control sample. Fitting second-order polynomials to the two populations in Figure 8, we calculated the difference in the IR excess between our dipper candidates to that of the K21 control

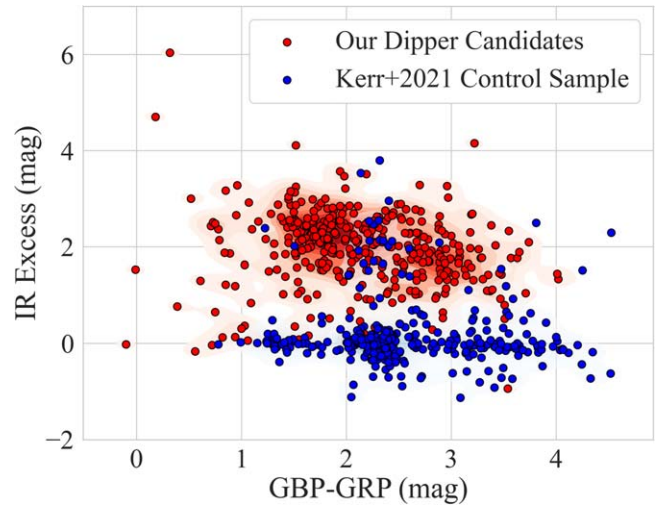


Figure 8. Scatter and contour plot illustrating the GBP - GRP color vs. IR excess for our dipper candidates (red points), which range between 2 and 42 Myr. A control sample of 392 sources from K21 are provided for comparison (blue points). A control star could be identified in the K21 sample for 93% of our dipper candidates. These comparison sources are close in age (within the K21 error bounds) to a given dipper candidate and have not been flagged as dipper variables in the past. We see that across all GBP - GRP values that our dipper candidates exhibit greater IR excess than the K21 control sample.

sample. Among sources where GBP - GRP = 1, the IR excess of our dipper candidates is 1.8 mag greater than that of the K21 sample. Similarly, among sources where GBP - GRP = 3 the IR excess of our dipper candidates is 1.6 mag greater than that of the K21 sample. The targets in the K21 control sample likely owe their optical redness to the fact that they are embedded in dust, which has a direct impact on their optical color but not IR color. Our population likely owes their IR excess to the presence of disks.

4.4. Morphology and Other Parameters as a Function of Age

We investigated for correlations between both the age and light-curve morphology of our dipper candidates, as well as correlations between temperature and light-curve morphology. In the top row of Figure 9, we observe a stochastic relationship between stellar age (in Myr) and both the flux asymmetry (left panel) and periodicity (right panel) metrics. Similarly, in the bottom row of Figure 9, we observe a stochastic relationship between the effective temperature and both the flux asymmetry (left panel) and periodicity (right panel) metrics. In the bottom row, the points are color coded to reflect the true color a human eye would see if observing a blackbody at that temperature.²²

We also compared the age distributions between the quasiperiodic and aperiodic subgroups for our catalog dipper stars ($M > 0.25$). The two age distributions are illustrated in the right column of Figure 10. Both distributions peak near a similar age, and a Kolmogorov-Smirnov test indicates no evidence that they are drawn from different distributions ($p \approx 0.5$). Therefore, we find no apparent relation between the periodicity values and age from this sample. It is worth noting that McGinnis et al. (2015) performed an analysis on a sample of dipper stars from NGC 2264, which were observed during two different epochs separated by three years. They showed that the light-curve morphology of dipper stars can change

²² <http://www.vendian.org/mncharity/dir3/blackbody/>

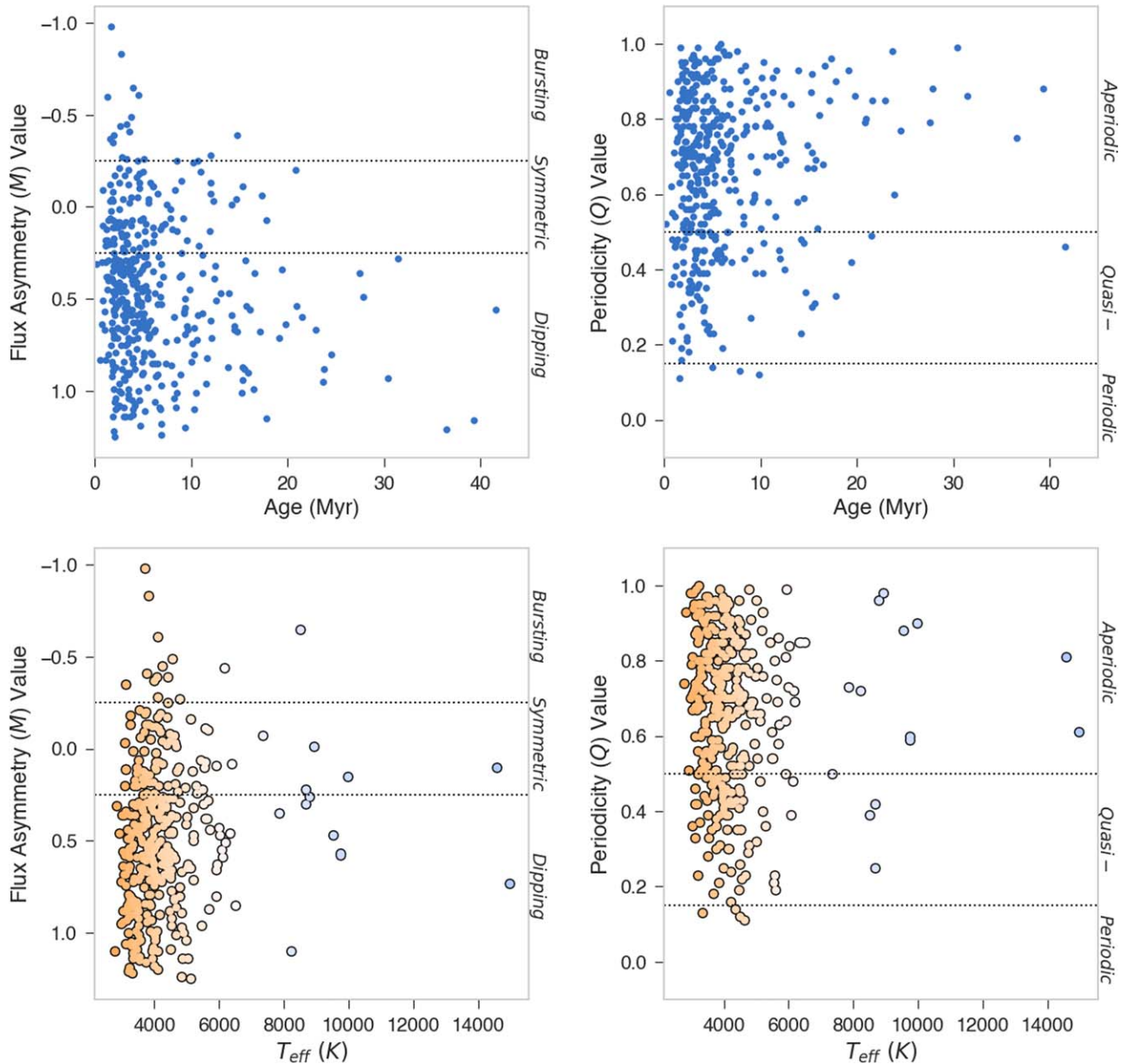


Figure 9. Stellar ages (Myr) determined in this work by the *Sagitta* neural network (as described by McBride et al. 2021) plotted against the calculated flux asymmetry metric, M (upper left), and against the calculated periodicity metric, Q (upper right). In the bottom panels, we plot T_{eff} against the M and Q metrics. The points are the true color a human eye would see if viewing a blackbody of that temperature (pixel red, green, blue (RGB) values are obtained from <http://www.vendian.org/mncharity/dir3/blackbody/>). We find no clear correlations between age or temperature of the source and the variability metrics of the catalog sources.

from periodic to aperiodic within timescales as short as three years. Given that stars move between periodic and aperiodic accretion regimes on timescales much shorter than their pre-main-sequence evolution, we do not expect to observe an appreciable difference in the age distribution between aperiodic and periodic systems, as shown in Figure 10.

We also investigated if the IR excess was more significant among the younger dipper candidates in our sample. As shown in Figure 11, no such evidence for a correlation between enhanced IR excess and age was found. In the left panel, we illustrate optical color ($\text{GBP} - \text{GRP}$) versus IR excess for dipper candidates with ages < 10 Myr, while the right panel illustrates this same parameter space for the sources with ages > 10 Myr. In both panels, we illustrate the *K21* control set (described in Section 4.3) for comparison. We note no

significant change in the IR excess as a function of age among our dipper candidate sample. This indicates that, regardless of age, our dipper candidates tend to be found in disk-hosting environments.

5. Summary and Discussion

In this work, we have produced a catalog of 414 young stellar variables. The catalog includes 293 dipper stars, including 234 new detections, representing the largest sample of dipper stars to date (a nearly 50% increase in the number of new dippers in the literature). We would like to note that nine of our new detections in the Orion Nebula Cluster were simultaneous, independent discoveries with research led by Moulton et al. (2022).

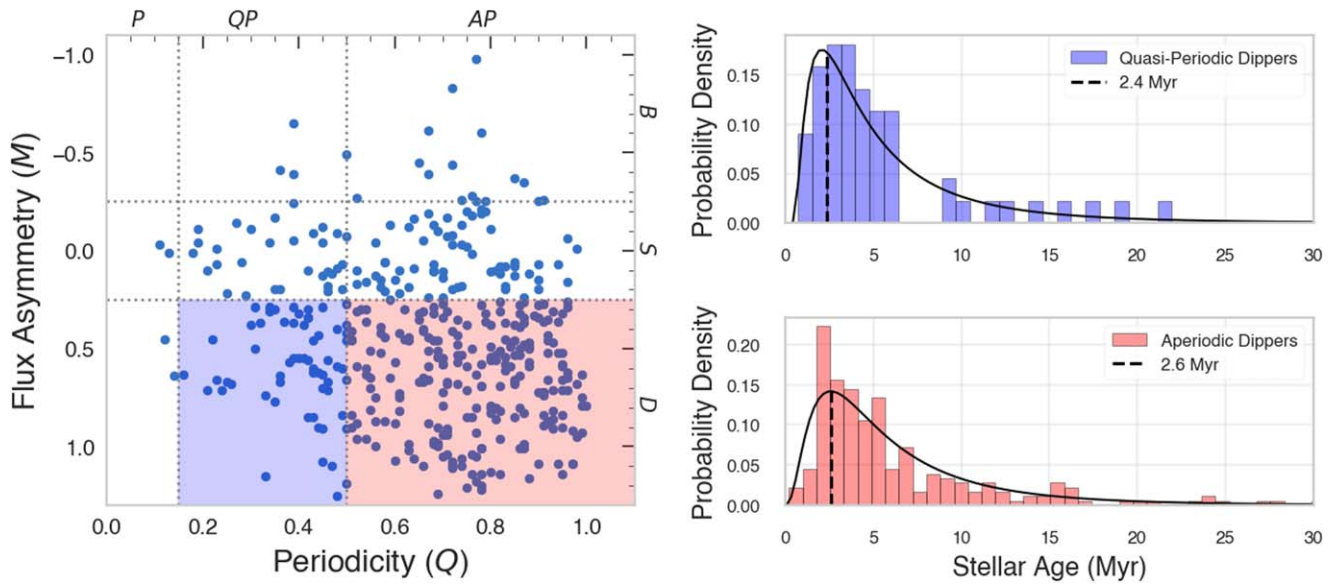


Figure 10. Sources from our catalog with ages determined by the *Sagitta* neural network (McBride et al. 2021). Left: we split the dipper candidates by their flux asymmetries and periodicity metrics, where quasiperiodic dipper stars are shown in the blue region, and aperiodic dipper stars are shown in the red region. Right: histograms of the ages calculated for the two groups of dipper stars, fit with log-normal distributions to identify the peak ages. The distribution of ages for the quasiperiodic dipper stars peaks at 2.4 Myr. Similarly, the age distribution of the aperiodic dipper stars peaks at 2.6 Myr. As we found in Figure 9, these histograms show no indication of a relation between periodicity values and age for our dipper stars.

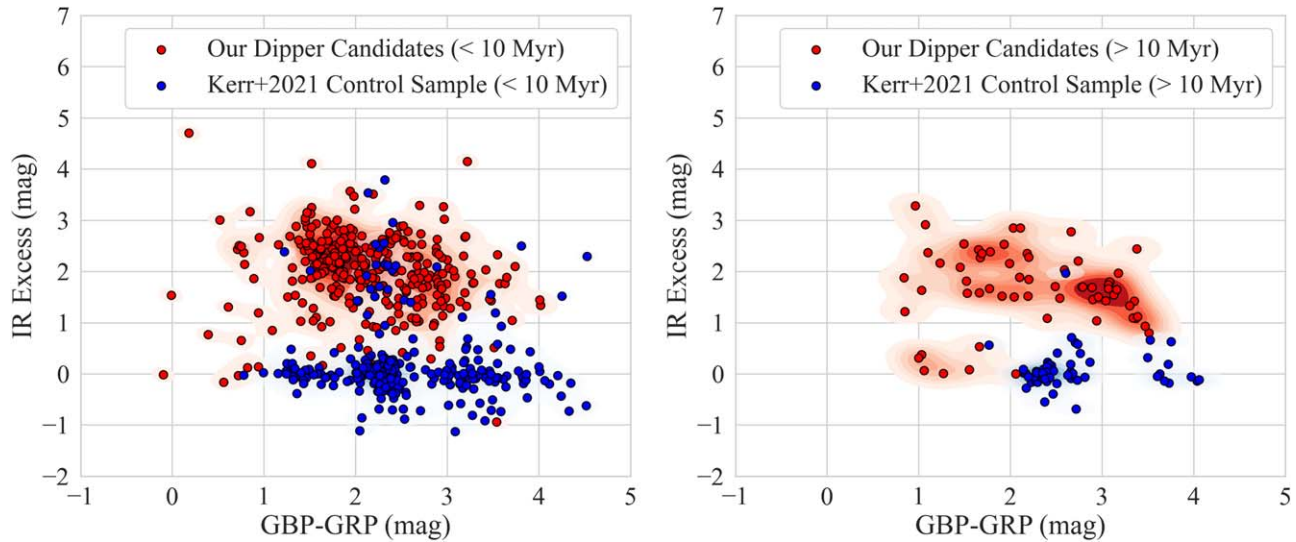


Figure 11. IR excess as a function of optical color ($GBP - GRP$) for our dipper candidates (red points). The *K21* control sample is provided for a comparison of similarly aged sources that do not display dipper-like variability (blue points). Sources are split into two groups: < 10 Myr (left) and > 10 Myr (right). Regardless of the age division shown, we see that across all $GBP - GRP$ values, our dipper candidates exhibit greater IR excess than the *K21* control sample. Further, when divided by age, the distribution of our dipper candidates in this parameter space does not change appreciably. This suggests that the older stars in our sample may retain their disks despite being older than the nominal disk dispersal timescale of $\sim 1-3$ Myr (Mamajek 2009).

Our new catalog sources have not been included in previously published dipper catalogs (e.g., Morales-Calderón et al. 2011; Cody et al. 2014; Rodríguez et al. 2017; Moulton 2020; Nardiello 2020; Rebull et al. 2020; Tajiri et al. 2020; Roggero et al. 2021; Venuti et al. 2021). A larger sample like ours benefits researchers in characterizing variable stars, discovering and confirming the physical mechanisms driving their variability, and investigating correlations with light-curve morphology and other stellar properties. By creating this catalog, we hope to assist future census investigations of dipper stars.

We collected ages and associations for our catalog sources, confirming their youth. The variable sources in our sample exhibit a peak in the age distributions at 2.3 Myr and 2.9 Myr in the age estimates from the *Sagitta* neural network (McBride et al. 2021) and from *K21*, respectively.

While the light-curve morphology statistics of variable stars have been relatively well studied, correlations between these characteristics and stellar age have not. We observed that the burster light curves in our catalog were only found in younger systems, while our dipper sources encompass the entire population age range of 1–40 Myr. Given that we only identified 20 burster

light curves ($\approx 5\%$ of our catalog light curves), a larger sample of bursting light curves is required to provide more definitive evidence of such a correlation. Similarly, we find no strong correlations between either of the light-curve morphology metrics and stellar effective temperature.

Our investigation provides evidence that dipper stars are not purely confined to systems younger than the typical disk dispersal timescale of $\sim 1\text{--}3$ Myr (Mamajek 2009) (Figure 6). Moreover, we find that the older (>10 Myr) dipper candidates also exhibit IR excess akin to that of the younger (<10 Myr) dipper candidates (Figure 11), suggesting that the older stars in our sample have retained their disks despite their age.

Recent literature concerning statistical modeling of asymmetrical events in time-series data has identified potential avenues for future work in identifying and classifying dipper stars (Hillenbrand et al. 2022). Methods identified from such studies could improve measurements of flux asymmetry, M , as defined by Cody & Hillenbrand (2010). For example, Carcea & Serfling (2015) and Shelef & Schechtman (2019) employ ACFs based on Gini extremes of distributions, which would offer a more sophisticated approach to the mean function of the M value. Along with these methods, the autoregressive moving average (ARMA) models proposed by Trindade et al. (2010) could provide a quantitative method for identifying and classifying dippers if they can be successfully applied to TESS light curves.

Since we finalized our target selection, TESS has continued to observe young stellar associations, including ϵ Chamaeleontis (1–3 Myr) (Feigelson et al. 2003), the Taurus–Auriga star-forming region (~ 3 Myr) (e.g., Kraus & Hillenbrand 2009; Luhman 2018), the Perseus OB2 association (6 Myr) (de Zeeuw et al. 1999), and the Pleiades (125 Myr) (Stauffer et al. 1998). Additionally, observations are planned in 2022 for Cepheus Flare (11 Myr) (Kerr et al. 2021), Cerberus (30 Myr) (Kerr et al. 2021),

and Aquila (youngest stars: 1–2 Myr) (Rice et al. 2006). With the continued production of high-quality light curves by the SPOC, PATHOS, QLP, and CDIPS teams, future discoveries of dipper targets are expected to expand upon this work.

We thank Ann Marie Cody, Ronan Kerr, Adam Kraus, and Tyler Moulton for their helpful conversations. M.S.F. gratefully acknowledges support provided by NASA through Hubble Fellowship grant HST-HF2-51493.001-A awarded by the Space Telescope Science Institute, which is operated by the Association of Universities for Research in Astronomy, Inc., for NASA, under the contract NAS 5-26555. The research has made use of the SIMBAD and VizieR databases, operated at the CDS, Strasbourg, France, and of NASA’s Astrophysics Data System Abstract Service. Resources supporting this work were provided by the NASA High-End Computing (HEC) Program through the NASA Advanced Supercomputing (NAS) Division at Ames Research Center for the production of the SPOC data products.

Facilities: TESS, Gaia DR2, Gaia EDR3, ADS.

Software: Astropy²³ (Astropy Collaboration et al. 2018), LcTools²⁴ (Schmitt et al. 2019; Schmitt & Vanderburg 2021), SciPy (Virtanen et al. 2020), Pandas (McKinney 2010), Matplotlib (Hunter 2007), Numpy (van der Walt et al. 2011), Lightkurve version 2.0.10 (Lightkurve Collaboration et al. 2018), Astroquery (Ginsburg et al. 2019), Astrocut (TESScut) (Basseur et al. 2019), Astrobases version 0.5.3 (Bhatti et al. 2017), cdips-pipeline (Bhatti et al. 2019), eleanor (Feinstein et al. 2019).

Appendix

Table 1 displays the first 10 entries of our stellar variable catalog, which includes 234 new dipper stars. The catalog is ordered by T_{mag} and the columns are described as follows:

²³ <http://www.astropy.org>

²⁴ <https://sites.google.com/a/lctools.net/lctools>

Table 1
Variable Star Catalog

	(1)	(2)	(3)	(4)	(5)	(6)	(7)	(8)	(9)	(10)	(11)
	TIC	Gaia DR2 ID	R.A. (deg)	Decl. (deg)	T_{mag} (mag)	Gaia mag (mag)	GBP (mag)	GRP (mag)	Vmag (mag)	T_{eff} (K)	Lum (L_{\odot})
0	355821272	445235933612724864	54.5043	55.1709	7.2	7.56	7.87	7.12	7.66	9966	NaN
1	240660823	391273208592115712	9.0644	48.5558	7.6	7.48	7.45	7.55	7.52	14580	NaN
2	390896668	487546103123764736	52.1633	62.4930	7.6	8.09	8.48	7.54	8.31	8914	NaN
3	347007416	420875841188703360	0.8631	55.5509	8.0	7.89	7.89	7.90	7.94	NaN	NaN
4	470475885	272403735203771264	66.3523	53.4153	8.7	9.09	9.48	8.54	9.33	NaN	NaN
5	51288359	5937028989511111680	251.9642	-51.7678	8.8	8.91	9.01	8.62	9.06	14955	NaN
6	406956018	429411727913975552	1.5058	60.8672	9.0	9.29	9.57	8.85	9.53	9747	NaN
7	201357489	223935338503901952	57.4014	38.9821	9.1	9.46	9.64	8.93	9.67	8665	87.99
8	376088043	540216042984524800	3.4191	77.0364	9.1	9.58	9.86	8.97	9.77	5718	NaN
9	159089190	3315807764324564352	88.5125	1.6728	9.1	9.84	10.29	8.87	10.11	NaN	NaN
	(12)	(13)	(14)	(15)	(16)	(17)	(18)	(19)	(20)	(21)	
	Stellar Radius (R_{\odot})	Log g (dex)	LC Source	Sector	M	Q	Variability	Known Dipper	Ages Kerr+2021 (Myr)	Ages Our Work (Myr)	
0	19.20	NaN	SPOC	19	0.15	0.90	AS	NaN	NaN	6.1	
1	NaN	NaN	QLP	17	0.10	0.81	AS	NaN	NaN	2.4	
2	22.89	NaN	SPOC	18	-0.01	0.98	AS	NaN	NaN	7.5	
3	NaN	NaN	QLP	17	0.35	0.92	AD	N	NaN	3.4	
4	NaN	NaN	SPOC	19	0.13	0.85	AS	NaN	NaN	8.5	
5	NaN	NaN	SPOC	12	0.73	0.61	AD	N	NaN	7.4	
6	30.41	NaN	QLP	18	0.57	0.60	AD	N	NaN	8.1	
7	4.16	3.54	QLP	18	0.30	0.42	QD	N	NaN	3.9	
8	NaN	NaN	QLP	18	0.44	0.63	AD	N	NaN	4.4	
9	NaN	NaN	QLP	6	0.75	0.61	AD	N	NaN	3.2	

Note. See the [Appendix](#) for a list of column descriptions.

(This table is available in its entirety in machine-readable form.)

1. *TIC ID*—TESS source identifier
2. *Gaia DR2 ID*—Gaia Data Release 2 source identifier
3. *RA*—Right ascension
4. *DEC*—Declination
5. *Tmag*—TESS magnitude
6. *Gaia mag*—Gaia DR2 magnitude
7. *GBP*—Gaia BP magnitude
8. *GRP*—Gaia RP magnitude
9. *Vmag*—*V* magnitude from TIC data
10. *Teff*—Effective temperature (K)
11. *Lum*—Luminosity (L_{\odot})
12. *Stellar Radius*—Stellar radius (R_{\odot})
13. *Logg*—Log of surface gravity (cm s^{-2})
14. *LC Source*—Source of the pregenerated light curve
15. *Sector*—TESS observation sector
16. *M*—Flux asymmetry “*M*” value
17. *Q*—Periodicity “*Q*” value
18. *Variability*—The variability classification of the star based on the *M* and *Q* light-curve morphology values. For periodicity: *A* = aperiodic, *Q* = quasiperiodic, *P* = periodic. For flux asymmetry: *D* = dipping, *S* = symmetric, *B* = bursting
19. *Known Dipper*—Indicates whether the star was classified as a dipper variable in previous investigations. Sources

that are not classified as dippers (those exhibiting predominately bursting or symmetric variability) are exempt from this classification parameter. *Y* = previously detected dipper. *N* = not previously detected (new detection in this study). NaN = source is not a dipper variable

20. *Ages Kerr+2021 (Myr)*—Stellar age in Myr for the variable star, as determined by [K21](#)
21. *Ages Our Work (Myr)*—Stellar age in Myr for the variable star, as determined by the Sagitta neural network ([McBride et al. 2021](#))

ORCID iDs

Benjamin K. Capistrant  <https://orcid.org/0000-0002-4592-8799>

Melinda Soares-Furtado  <https://orcid.org/0000-0001-7493-7419>

Andrew Vanderburg  <https://orcid.org/0000-0001-7246-5438>

Marina Kounkel  <https://orcid.org/0000-0002-5365-1267>

Saul A. Rappaport  <https://orcid.org/0000-0003-3182-5569>

Brian P. Powell  <https://orcid.org/0000-0003-0501-2636>

Robert Gagliano  <https://orcid.org/0000-0002-5665-1879>

Thomas Jacobs  <https://orcid.org/0000-0003-3988-3245>

Veselin B. Kostov  <https://orcid.org/0000-0001-9786-1031>
 Martti H. Kristiansen  <https://orcid.org/0000-0002-2607-138X>
 Daryll M. LaCourse  <https://orcid.org/0000-0002-8527-2114>
 Allan R. Schmitt  <https://orcid.org/0000-0002-5034-0949>
 Hans Martin Schwengeler  <https://orcid.org/0000-0002-1637-2189>
 Ivan A. Terentev  <https://orcid.org/0000-0002-0654-4442>

References

- Aigrain, S., Hodgkin, S. T., Irwin, M. J., Lewis, J. R., & Roberts, S. J. 2015, *MNRAS*, **447**, 2880
- Alencar, S. H. P., Teixeira, P. S., Guimarães, M. M., et al. 2010, *A&A*, **519**, A88
- Alencar, S. H. P., Bouvier, J., Donati, J.-F., et al. 2018, *A&A*, **620**, A195
- Ansdell, M., Gaidos, E., Rappaport, S. A., et al. 2016, *ApJ*, **816**, 69
- Astropy Collaboration, Price-Whelan, A. M., Sipőcz, B. M., et al. 2018, *AJ*, **156**, 123
- Auvergne, M., Bodin, P., Boisdard, L., et al. 2009, *A&A*, **506**, 411
- Baglin, A., Auvergne, M., Boisdard, L., et al. 2006, in 36th COSPAR Scientific Assembly (Beijing: COSPAR), 3749
- Bhatti, W., Bouma, L., & Yee, S. 2019, waqasbhatti/cdips-pipeline: cdips-pipeline v0.1.0, v0.1.0, Zenodo, doi:10.5281/zenodo.3370324
- Bhatti, W., Bouma, L. G., & Wallace, J. 2017, waqasbhatti/astrobases: astrobases v0.5.3, v0.5.3, Zenodo, doi:10.5281/zenodo.1011188
- Bodman, E. H. L., Quillen, A. C., Ansdell, M., et al. 2017, *MNRAS*, **470**, 202
- Borucki, W. J., Koch, D., Basri, G., et al. 2010, *Sci*, **327**, 977
- Bouma, L. G., Hartman, J. D., Bhatti, W., Winn, J. N., & Bakos, G. Á. 2019, *ApJS*, **245**, 13
- Bouvier, J., Alencar, S. H. P., Boutelier, T., et al. 2007, *A&A*, **463**, 1017
- Bouvier, J., Chelli, A., Allain, S., et al. 1999, *A&A*, **349**, 619
- Bouvier, J., Grankin, K. N., Alencar, S. H. P., et al. 2003, *A&A*, **409**, 169
- Brasseur, C. E., Phillip, C., Fleming, S. W., Mullally, S. E., & White, R. L. 2019, Astrocut: Tools for creating cutouts of TESS images, Astrophysics Source Code Library, ascl:1905.007
- Bredall, J. W., Shappee, B. J., Gaidos, E., et al. 2020, *MNRAS*, **496**, 3257
- Carcea, M., & Serfling, R. 2015, *J. Time Ser. Anal.*, **36**, 817
- Cargile, P. A., James, D. J., & Jeffries, R. D. 2010, *ApJL*, **725**, L111
- Cody, A. M., & Hillenbrand, L. A. 2010, *ApJS*, **191**, 389
- Cody, A. M., & Hillenbrand, L. A. 2018, *AJ*, **156**, 71
- Cody, A. M., Stauffer, J., Baglin, A., et al. 2014, *AJ*, **147**, 82
- Cutri, R. M., Wright, E. L., Conrow, T., et al. 2021, *yCat*, II/328
- Damiani, F., Prisinzano, L., Pillitteri, I., Micela, G., & Sciortino, S. 2019, *A&A*, **623**, A112
- de Zeeuw, P. T., Hoogerwerf, R., de Bruijne, J. H. J., Brown, A. G. A., & Blaauw, A. 1999, *AJ*, **117**, 354
- Favata, F., Flaccomio, E., Reale, F., et al. 2005, *ApJS*, **160**, 469
- Fazio, G. G., Hora, J. L., Allen, L. E., et al. 2004, *ApJS*, **154**, 10
- Feigelson, E. D., Lawson, W. A., & Garmire, G. P. 2003, *ApJ*, **599**, 1207
- Feinstein, A. D., Montet, B. T., Foreman-Mackey, D., et al. 2019, *PASP*, **131**, 094502
- Frasca, A., Manara, C. F., Alcalá, J. M., et al. 2020, *A&A*, **639**, L8
- Gaia Collaboration, Brown, A. G. A., Vallenari, A., et al. 2018, *A&A*, **616**, A1
- Gaia Collaboration, Brown, A. G. A., Vallenari, A., et al. 2021, *A&A*, **649**, A1
- Ginsburg, A., Sipőcz, B. M., Brasseur, C. E., et al. 2019, *AJ*, **157**, 98
- Hedges, C., Hodgkin, S., & Kennedy, G. 2018, *MNRAS*, **476**, 2968
- Hillenbrand, L. A., Kiker, T. J., Gee, M., et al. 2022, *AJ*, **163**, 263
- Howell, S. B., Sobeck, C., Haas, M., et al. 2014, *PASP*, **126**, 398
- Huang, C. X., Vanderburg, A., Pál, A., et al. 2020a, *RNAAS*, **4**, 204
- Huang, C. X., Vanderburg, A., Pál, A., et al. 2020b, *RNAAS*, **4**, 206
- Hunter, J. D. 2007, *CSE*, **9**, 90
- Jenkins, J. M., Twicken, J. D., McCauliff, S., et al. 2016, *Proc. SPIE*, **9913**, 99133E
- Kerr, R. M. P., Rizzuto, A. C., Kraus, A. L., & Offner, S. S. R. 2021, *ApJ*, **917**, 23
- Kochanek, C. S., Shappee, B. J., Stanek, K. Z., et al. 2017, *PASP*, **129**, 104502
- Kounkel, M., Covey, K., & Stassun, K. G. 2020, *AJ*, **160**, 279
- Kounkel, M., Covey, K., Suárez, G., et al. 2018, *AJ*, **156**, 84
- Kraus, A. L., & Hillenbrand, L. A. 2009, *ApJ*, **704**, 531
- Kraus, A. L., Shkolnik, E. L., Allers, K. N., & Liu, M. C. 2014, *AJ*, **147**, 146
- Kristiansen, M. H. K., Rappaport, S. A., Vanderburg, A. M., et al. 2022, *PASP*, **134**, 074401
- Lightcurve Collaboration, Cardoso, J. V. d. M., Hedges, C., et al. 2018, Lightkurve: Kepler and TESS time series analysis in Python, Astrophysics Source Code Library, ascl:1812.013
- Luhman, K. L. 2018, *AJ*, **156**, 271
- Mamajek, E. E. 2009, in AIP Conf. Proc. 1158, Exoplanets and Disks: Their Formation and Diversity, ed. T. Usuda, M. Tamura, & M. Ishii (Melville: AIP), 3
- Mann, A. W., Johnson, M. C., Vanderburg, A., et al. 2020, *AJ*, **160**, 179
- McBride, A., Lingg, R., Kounkel, M., Covey, K., & Hutchinson, B. 2021, *AJ*, **162**, 282
- McGinnis, P. T., Alencar, S. H. P., Guimarães, M. M., et al. 2015, *A&A*, **577**, A11
- McKinney, W. 2010, in Proc. of the 9th Python in Science Conf., ed. S. van der Walt & J. Millman (Austin, TX: SciPy), 56, <https://conference.scipy.org/proceedings/scipy2010/mckinney.html>
- Morales-Calderón, M., Stauffer, J. R., Hillenbrand, L. A., et al. 2011, *ApJ*, **733**, 50
- Moulton, T. 2020, Bachelor's thesis, Harvard Univ., <https://dash.harvard.edu/handle/1/37364679>
- Moulton, T., Hodgkin, S. T., & Smith, G. D. 2022, *MNRAS*, submitted
- Nardiello, D. 2020, *MNRAS*, **498**, 5972
- Nardiello, D., Borsato, L., Piotto, G., et al. 2019, *MNRAS*, **490**, 3806
- Oelkers, R. J., & Stassun, K. G. 2018, *AJ*, **156**, 132
- Oelkers, R. J., & Stassun, K. G. 2019, *RNAAS*, **3**, 8
- Pecaut, M. J., & Mamajek, E. E. 2013, *ApJS*, **208**, 9
- Pepper, J., Pogge, R. W., DePoy, D. L., et al. 2007, *PASP*, **119**, 923
- Powell, B. P., Kostov, V. B., Rappaport, S. A., et al. 2021, *AJ*, **161**, 162
- Powell, B. P., Kruse, E., Montet, B. T., et al. 2022, *RNAAS*, **6**, 111
- Rebull, L. M., Stauffer, J. R., Cody, A. M., et al. 2015, *AJ*, **150**, 175
- Rebull, L. M., Stauffer, J. R., Cody, A. M., et al. 2020, *AJ*, **159**, 273
- Rice, E. L., Prato, L., & McLean, I. S. 2006, *ApJ*, **647**, 432
- Ricker, G. R., Winn, J. N., Vanderspek, R., et al. 2015, *JATIS*, **1**, 014003
- Rodriguez, J. E., Ansdell, M., Oelkers, R. J., et al. 2017, *ApJ*, **848**, 97
- Roggero, N., Bouvier, J., Rebull, L. M., & Cody, A. M. 2021, *A&A*, **651**, A44
- Schmitt, A., & Vanderburg, A. 2021, arXiv:2103.10285
- Schmitt, A. R., Hartman, J. D., & Kipping, D. M. 2019, arXiv:1910.08034
- Schmitt, J. R., Tokovinin, A., Wang, J., et al. 2016, *AJ*, **151**, 159
- Shelef, A., & Schechtman, E. 2019, *Stat. Papers*, **60**, 687
- Stassun, K. G., Oelkers, R. J., Pepper, J., et al. 2018, *AJ*, **156**, 102
- Stauffer, J., Cody, A. M., McGinnis, P., et al. 2015, *AJ*, **149**, 130
- Stauffer, J. R., Schultz, G., & Kirkpatrick, J. D. 1998, *ApJL*, **499**, L199
- Stellingwerf, R. F. 1978, *ApJ*, **224**, 953
- Tajiri, T., Kawahara, H., Aizawa, M., et al. 2020, *ApJS*, **251**, 18
- Trindade, A. A., Zhu, Y., & Andrews, B. 2010, *J. Stat. Comput. Simul.*, **80**, 1317
- van der Walt, S., Colbert, S. C., & Varoquaux, G. 2011, *CSE*, **13**, 22
- Vanderburg, A., & Johnson, J. A. 2014, *PASP*, **126**, 948
- Venuti, L., Cody, A. M., Rebull, L. M., et al. 2021, *AJ*, **162**, 101
- Virtanen, P., Gommers, R., Oliphant, T. E., et al. 2020, *NatMe*, **17**, 261
- Werner, M. W., Roellig, T. L., Low, F. J., et al. 2004, *ApJS*, **154**, 1
- Wheatley, P. J., West, R. G., Goad, M. R., et al. 2018, *MNRAS*, **475**, 4476